Chemical routes to materials

UV-light-assisted preparation of MoO$_{3-x}$/Ag NPs film and investigation on the SERS performance

Zhiqiang Niu[1], Canliang Zhou[1], Jiawei Wang[1], Yinghao Xu[1], Chenjie Gu[1,*], Tao Jiang[1,*], Shuwen Zeng[2], Yonghui Zhang[3], Diing Shenp Ang[4], and Jun Zhou[1]

[1] Institute of Photonics, Ningbo University, 818 Feng Hua Road 315211, Ningbo, China

[2] XLIM Research Institute, UMR 7252, CNRS/University of Limoges, Avenue Albert Thomas, 87060 Limoges, France

[3] School of Electronic and Information Engineering, Heibei University of Technology, 5340 Xiping Road, Tianjin 300401, China

[4] School of Electrical and Electronic Engineering, Nanyang Technological University, 50 Nanyang Avenue, Singapore 639798, Singapore

ABSTRACT

Surface-enhanced Raman scattering (SERS) technique is a powerful spectrum analysis technique for the ultra-low molecular trace detection. Conventionally, noble metals like silver (Ag) and gold (Au) are used to prepare the SERS substrates; however, limitations of complicated experimental designs and sophisticated process steps impede their wide applications in practice. Recently, metal oxides arise as a promising material for SERS application, but relatively weak Raman signal enhancement and poor material stability still pose as a challenge. Here, a UV-light-assisted fabrication of MoO$_{3-x}$/silver nanoparticles (MoO$_{3-x}$/Ag NPs) film is proposed. In the experiment, the sub-transition-metal-oxide of MoO$_{3-x}$ was used as the Raman chemical enhancement substrate as well as the reducing agent. Through the spin-coating of MoO$_{3-x}$ layer on the silicon substrate and UV-light-assisted reduction of silver nitride (AgNO$_3$) on the MoO$_{3-x}$ layer, a novel MoO$_{3-x}$/Ag NPs one-layer film was fabricated. Using the Rhodamine B (RhB) as the Raman reporter, SERS measurement shows that enhancement factor (EF) of 1.195×10^6 could be achieved. Moreover, a Raman signal amplifying strategy is further demonstrated by constructing MoO$_{3-x}$/Ag NPs multi-layer films. And result evidences that maximum gain of 2.07 for the RhB Raman peak at 1280 cm^{-1} can be obtained on the MoO$_{3-x}$/Ag NPs three-layer film when referred to that on the MoO$_{3-x}$/Ag NPs one-layer film. Meanwhile, the EF of the MoO$_{3-x}$/Ag NPs three-layer film is also improved to 2.985×10^6, giving the minimum detectable concentration of 10^{-9} M.

Address correspondence to E-mail: guchenjie@nbu.edu.cn; jiangtao@nbu.edu.cn

Introduction

Surface-enhanced Raman scattering (SERS) technique, as a simple, rapid, non-destructive and highly sensitive spectroscopic analysis method, has gained enormous interests for the ultra-low trace detection of chemical composites, biological molecules and environmental contaminants [1–4]. Generally, noble metals like silver (Ag) and gold (Au) are the prior choice materials to prepare the SERS substrates, which are attributed to their excellent electromagnetic enhancement mechanism (EM) produced by the surface plasmons [5–15]. However, in order to achieve strongly confined surface electromagnetic field or "hot spots", and subsequently promote the SERS detection capability, careful experiment designs and preparation of the noble-metal nanostructures are required [5, 6]. Up to date, a large number of noble metal structures with various morphologies that prepared by chemical synthesis or semiconductor fabrication techniques have been reported [16–23]. For example, Liz-Marzán et al. demonstrated a scalable method of preparing the gold nanoparticle plasmonic superlattices through template-assisted assembly of gold nanospheres, which showed tunable plasmon modes from near-infrared to visible light and potentially extended the selection of probe laser [24]. In the meanwhile, Xia et al. addressed the facile synthesis of sharp corners and edges silver nanocubes in aqueous environment. From the Raman measurement, it indicated that these nanocubes showed strong SERS activities [25]. Other than that, Yang et al. fabricated the noble metal functionalized Si nanorod arrays with the reactive ion etching, metal deposition and chemical etching processes, which demonstrated excellent spatially uniform SERS performance throughout the whole substrate [26]. Nevertheless, in spite of the fact that attractive SERS performances have been obtained on numerous nanostructures, and the enhancement factors (EFs) can easily reach as high as 10^5–10^8, chemical synthesis methods always involve the proper using of active surfactants and accurate control of the reaction conditions to guarantee the uniformity and reproducibility of the nanostructures, while the semiconductor fabrication techniques, like metal physical deposition and etching method, usually consume time and cost a lot. Moreover, surfactants are certain kinds of surface-active molecules, in the chemical synthesis procedure, they selectively attach to specific crystal surfaces to help the controlled growth of the nanostructures; however, these molecules also inevitably occupy the valuable surficial area on the nanostructures. During the SERS measurement, the clean area left on the nanoparticle to adsorb the analytes is significantly reduced; consequently, the SERS performance is severely deteriorated [27, 28].

Most recently, studies on transition metal oxides, transition metal chalcogenides and two-dimensional materials have evidenced that non-noble metal surface could also provide SERS enhancement through the chemical enhancement mechanism (CM) [29–31]. Since CM strongly depends on the defect level-assisted charge transfer (CT) between the substrate and molecules, defect engineering is essentially important to facilitate the CT [32, 33]. Presently, decent SERS performance has been reported on the materials like Cu_2O, Cu_2S, MoS_2, TiO_2 and WS_2, and lately, outstanding SERS characteristics were also observed on defective molybdenum oxide [34–38]. For example, John et al. synthesized urchin-like MoO_3 nanostructure through the chemical bath deposition method. Experimental results indicated that the urchin-like MoO_3 nanostructures were rich in oxygen vacancies. And in the Raman measurement, relying on the efficient CT supported by the defect levels, the MoO_3 nanostructures achieved a relatively high EF of 10^5 and a lower limit of detection (LOD) of 10^{-7} M by using the Rhodamine 6 G (R6G) as the Raman reporter [39]. Moreover, another achievement reported by Liu et al, presented the synthesis of molybdenum oxide nanoparticles through defect engineering for SERS detection. In the experiment, the bulk MoS_2 was oxidized into MoO_2, MoO_{3-x} and MoO_3 by controlling the reaction time, respectively. And SERS measurement revealed that the most defective products-MoO_2 showed the superior SERS performance with the detection limit was as low as 5×10^{-8} M [40]. Besides, defect tuning in the MoO_3 through hydrogen ion (H^+) insertion as well as weak chemical reduction reaction with poly (ethylene oxide), ascorbic acid or dopamine etc. was also widely discussed, and results evidenced that introducing high level defect density in the molybdenum oxide can significantly promote the CT process, producing admirable SERS performance [40–44]. At this stage, it is notable that non-noble-metal materials also show attractive SERS performance; however, compared to most of the noble-metal based SERS

substrates, the EFs obtained on the majority of non-noble metal materials are still not high enough for ultra-sensitive molecule detection, especially for molecules that the molecular orbits are not well aligned with the non-noble-metal materials, which further retards the CT. In view of the above situation, SERS substrates contain both noble-metal materials and oxides have attracted massive attentions. In order to make use of both EM and CM, MoO_3-Au hybrid substrate, MoO_x-AuNSs composites, TiO_2-Au nanocomposites and TiO_2-Ag hybrid structure, etc., has been reported in the studies, and Raman measurements indicate that they own excellent SERS performance [45–48]. Nevertheless, it should be mentioned that complex chemical synthesis or process steps are required to prepare these combined substrates, which weaken their advantages on admirable EFs.

Herein, we report a facile strategy to prepare an attractive SERS substrate by developing the MoO_{3-x}/ silver nanoparticles (MoO_{3-x}/Ag NPs) film. In this work, MoO_{3-x}, a relatively stable sub-transition-metal-oxide, is used as a Raman chemical enhancement substrate as well as the reducing agent. Controlled preparation of MoO_{3-x}/Ag NPs one-layer film is obtained through the spin-coating of MoO_{3-x} film on the silicon substrate and UV-light-assisted reduction of silver nitride ($AgNO_3$) on the MoO_{3-x} film. The Raman performance of the prepared MoO_{3-x}/Ag NPs one-layer film is evaluated by using the Rhodamine B (RhB) as the reporter. Experimental results reveal that the enhancement factor of the MoO_{3-x}/Ag NPs one-layer film can reach 1.195×10^6, which is produced by the synergetic Raman signal enhancement of EM and CM [49]. More interestingly, a kindly of multi-stage Raman signal amplifying strategy is realized by constructing MoO_{3-x}/Ag NPs multi-layer film. Raman measurement result evidences that maximum gain of 2.07 at the RhB Raman peak of 1280 cm^{-1} can be obtained on MoO_{3-x}/Ag NPs three-layer film when compared to that measured on the MoO_{3-x}/Ag NPs one-layer film. In the meanwhile, the EF of the MoO_{3-x}/Ag NPs three-layer film is also improved to 2.985×10^6, giving the minimum detectable concentration of 10^{-9} M. All in all, this work offers a facile and effective method of prepare attractive SERS substrate, and it potentially enriches the selection of ultra-sensitive SERS sensor for molecular trace sensing application.

Materials and methods

Chemicals

RhB and $AgNO_3$ were purchased from Sigma-Aldrich. Aqueous ammonia ($NH_3 \cdot H_2O$), hydrogen peroxide (H_2O_2) and ethanol was obtained from Sinopharm Chemical Agent Co., Ltd. Molybdenyl acetylacetonate ($[CH_3COCH=C(O)CH_3]_2MoO_2$) was purchased from Shanghai Macklin Biochemical Co., Ltd. All chemicals in the experiment were of analytical purity and used without further purification. Milli-Q water (18.2 MΩ cm) was used throughout the whole experiment.

Sample preparation

Synthesis of MoO_{3-x} powder 0.1 g of molybdenyl acetylacetonate was first added into the mixed solution of distilled water (41 mL) and absolute ethanol (9 mL), then stirred for 1 h at room temperature [50]. Thereafter, the above mixture solution was added into a Teflon-lined stainless-steel autoclave and kept at 180 °C for 20 h. After the reaction was completed, the black products were collected by high speed centrifugation, washed with distilled water for three times, and finally dried at 50 °C in a vacuum oven. The morphology of the synthesized MoO_{3-x} was detected by SEM, and it showed cube-like nanostructure (Fig. S1(a) and (b), Supplementary Information).

Preparing the MoO_{3-x}/Ag NPs film the MoO_{3-x} film was prepared by a layer-by-layer method, which was schematically shown in Fig. 1. Firstly, the silicon substrate was cleaned by $NH_3 \cdot H_2O/H_2O_2/H_2O$ solution (1:1:5), thereafter, 20 μL of the prepared MoO_{3-x} ethanol solution (23 wt %) was dropped on the center of the silicon substrate, and then it was spin-coated on the substrate at 450 rpm for 100 s. This dropping and spin-coating procedures were repeated for 12 times to obtain a 200-nm MoO_{3-x} film (Fig. S1(c), Supplementary Information). Then, the substrates were annealed at 150 °C for 0.5 h in the air ambient to improve the adhesion. After that, 10 μL of $AgNO_3$ solution was drop-casted on the MoO_{3-x} film and then illuminated by 253.7-nm UV-light with the power of 10 mW·cm^{-2} for 2 h. During this period, Ag^+ ions were reduced to Ag NPs, and MoO_{3-x}/Ag NPs one-layer film was obtained [51]. Moreover, to build MoO_{3-x}/Ag NPs multi-layer film, additional

Figure 1 Schematic illustration of the preparation flows for fabricating the MoO_{3-x}/Ag NPs film.
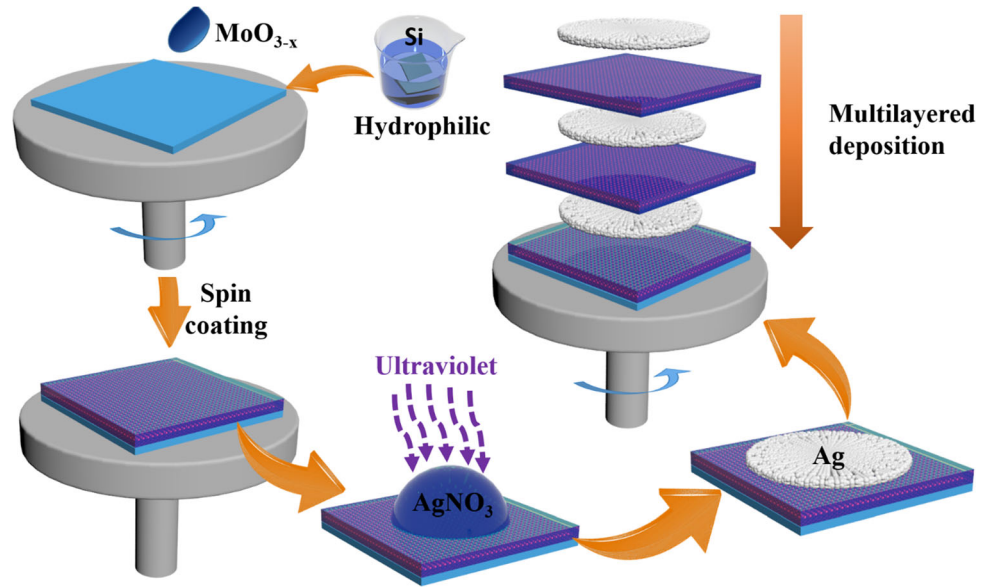
MoO_{3-x}/Ag NPs layers were sequentially prepared with the same procedure on the prior one.

Measurements and characterization

The sizes and morphologies of the samples were detected by SU-70 field emission scanning electron microscopy (Hitachi, Japan) under an accelerating voltage of 5 kV, and the object distance was 6 mm. The element energy-dispersive spectroscopy (EDS) spectra and element EDS mapping of the samples were also obtained on SU-70 FESEM equipped with EDAX (EDAX, USA). The optical absorption spectra of the products were recorded with a TU-1901 UV–Vis spectrometer (Shimadzu, Japan). The X-ray diffraction (XRD) spectra of the samples were identified on a D8 Advance diffraction meter equipped with a LynxEye XE detector (Bruker-AXS, Germany). X-Ray photoelectron spectroscopy (XPS) was measured by ESCALAB 250Xi (ThermoFisher, USA). The qualitative analysis for chemical identification was performed through high-resolution scan of the Mo3d spectral region. The binding energies (BE) and charge corrections were referenced to the C1s line at 284.8 eV. The SERS properties of the samples were examined by a Raman microscope equipped with a QE Pro spectrometer (Ocean Optics, USA) using a 532-nm semiconductor laser as the excitation source. The laser power on the sample was 1 mW, the integration time was 10 s, and the diameter of the spot size was 12.5 μm (100 × objective lens with numerical aperture of 0.8). All the analysis was performed at room temperature.
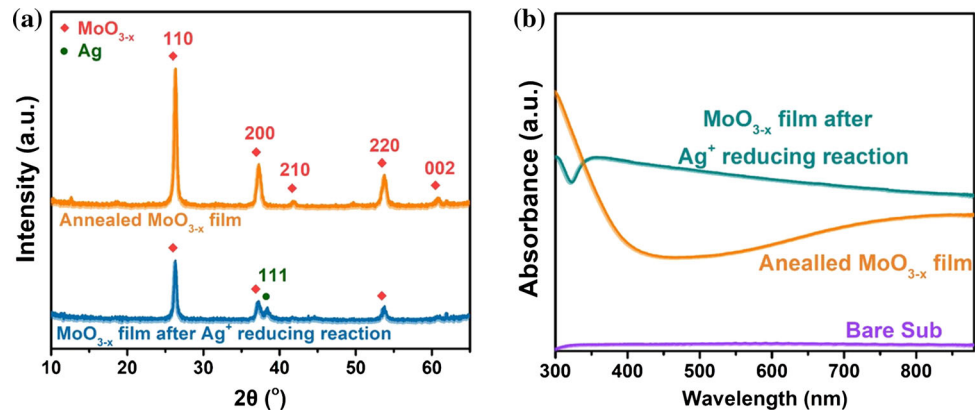
FDTD simulations

The numerical simulations were performed with the FDTD method. All the structures were excited by a planewave source with the wavelength from 370 to 682 nm. The permittivity of Ag was deduced from the Drude–Lorentz model fitted to the experimental data. In order to suppress the noise reflected or scattered from the simulated boundaries, the boundaries of the area were set to a perfectly matched layer.

Results and discussion

XRD analysis was first conducted to investigate the phase structures of the films. Figure 2a shows the XRD spectra of the annealed MoO_{3-x} film and the film after the Ag$^+$ reducing reaction under the UV-light illumination. Apparently, on the diffraction pattern of the annealed MoO_{3-x} film, peaks belong to the (110), (200), (210), (220) and (002) planes of the monoclinic MoO_3 can be observed (JCPDS No. 78-1069) [36], whereas extra peak around 38.1° only appears on the diffraction pattern collected on the film after the reducing reaction under the UV-light illumination, which can be assigned to the (111) plane of the Ag lattice (JCPDS No. 04-0783) and indicates the successful synthesis of the Ag NPs [52].

Moreover, to obtain the optical characteristics of the film, UV–Vis absorption spectra of the above two different films were collected and are shown in Fig. 2b. As it can be found on the annealed MoO_{3-x} film that, besides the strong absorption tail beyond the absorption edge (wavelength > 300 nm), weak absorption hump is also detected below the wavelength of 500 nm, which is considered to be closely related to the oxygen deficiency-induced small polarons [42, 53], while absorption curve collected on the film after the reducing reaction under the UV-light illumination exhibits a wide absorption envelope with the peak located around 370 nm. This unique absorption pattern is attributed to the strong interaction between the irregular Ag NPs and incident light [54].

SEM detections were then performed to investigate the morphologies of the nanoparticles on the UV-light illuminated film. Figure 3 shows the typical SEM images of Ag NPs obtained by using different concentrations of $AgNO_3$ solution from 0.18 to 1.8 mg mL^{-1}. It can be found that when the concentration of the $AgNO_3$ solution rises, which tends to provide more Ag^+ source during the reaction, the number and size of Ag NPs on the MoO_{3-x} film increases. To be more specific, on the MoO_{3-x} film dropped with 1.8 mg mL^{-1} of $AgNO_3$ solution, much denser and larger Ag NPs are synthesized. And SEM images of Ag NPs illustrate that Ag NPs show hydrangea-like shapes with notable walls on the surface, which ensures the generation of intensive surface electromagnetic field on the Ag NPs surface (Fig. S2(a) and (b), Supplementary Information). In addition, relatively small Ag NPs are also detected between those sizable Ag NPs, this structural advantage will further narrower the gaps between

the Ag NPs and ultimately generate strong "hot spots" [55].

Other than that, local element EDS mapping spectra were also collected and are shown in Fig. 4. Ag, N, Mo and O element are clearly detected (Fig. 4b–f), and from the Ag element mapping (Fig. 4b), it can be observed that Ag NPs irregularly distributed on the surface, which further confirms the formation of MoO_{3-x}/Ag NPs film under the UV-light illumination [56]. In addition, Mo element the film is conformally distributed on the surface; as an evidence, it can be inferred that CM also will be present during the SERS measurement [54].

The valence states of the elements in annealed MoO_{3-x} film and the MoO_{3-x}/Ag NPs film were identified by XPS analysis. Figure 5a shows the XPS survey spectra collected on the annealed MoO_{3-x} film, and it can be observed that six prominent peaks in the survey spectra are clearly shown, which can be indexed to Mo3d (232.07 eV), C1s (283.1 eV), Mo3p (395.8 and 413.2 eV), Mo3s (505.0 eV) and O1s (528.7 eV), respectively [36]. In the meanwhile, Fig. 5b illustrates the XPS survey spectra collected on the MoO_{3-x}/Ag NPs film, it evidences that, apart from the Mo3d, Mo3p, Mo3s and O1s peaks, $Ag3d_{5/2}$ (368.0 eV), $Ag3p_{3/2}$ (573.0 eV) and $Ag3p_{1/2}$ (604.0 eV) are also clearly shown. Moreover, XPS fine-scan spectra of the Mo element in the annealed MoO_{3-x} film and MoO_{3-x}/Ag NPs film were performed and are shown in Fig. 5c and d, respectively. Both of them show typical four-peak envelopes. Thereafter, in order to further clarify the valence state of the Mo element in the film, deconvolution operations were performed on the two core level spectra of Mo3d. As it can be found in Fig. 5c and d that four-peak-shaped Mo3d spectra could be well fitted into three spin–
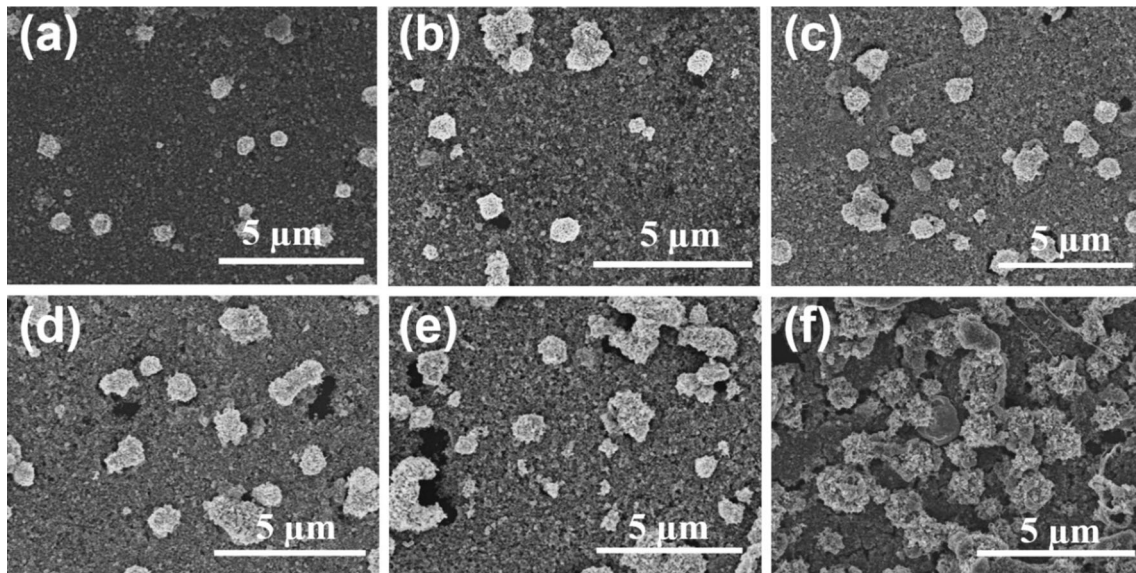
Figure 3 SEM images of MoO_{3-x}/Ag NPs film prepared with different concentrations of $AgNO_3$ solution: **a** 0.18 mg mL-1, **b** 0.36 mg mL^{-1}, **c** 0.45 mg mL^{-1}, **d** 0.6 mg mL^{-1}, **e** 0.9 mg mL^{-1}, **f** 1.8 mg mL^{-1}.
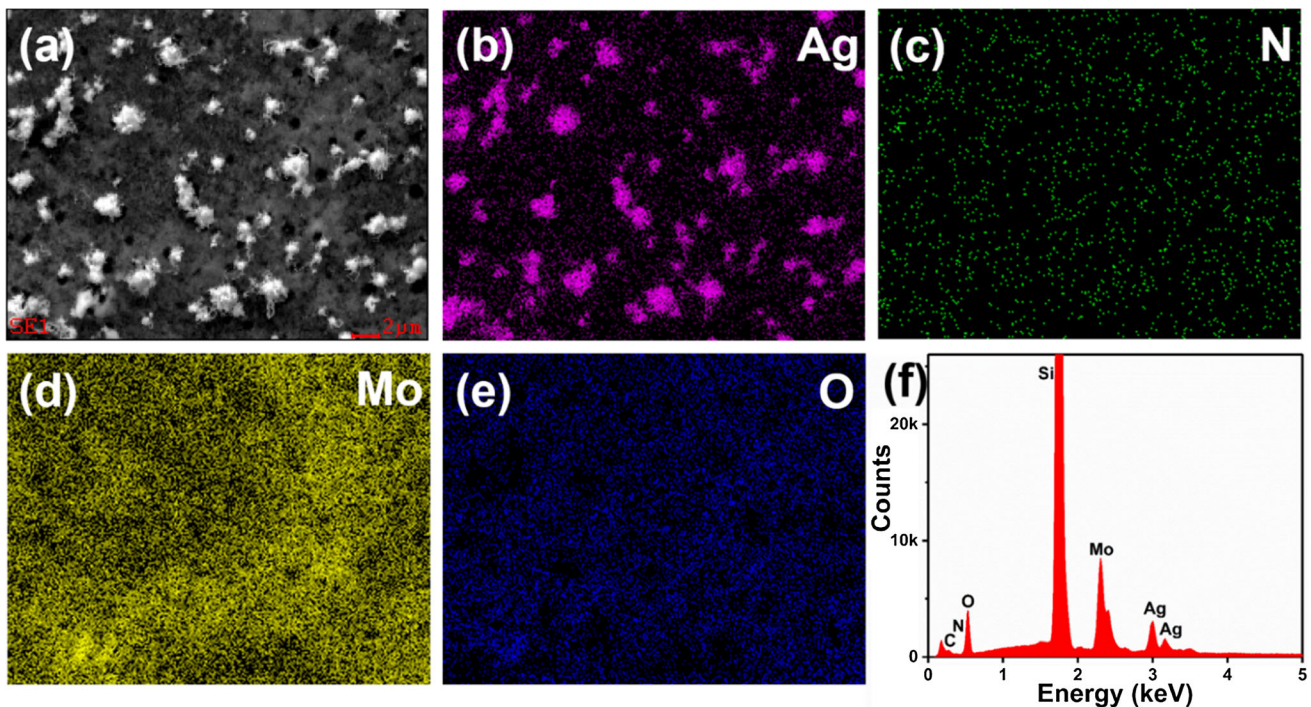

Figure 4 **a** SEM image of the film; the corresponding elements mapping, **b** Ag, **c** N, **d** Mo, **e** O and **f** the EDS spectra of the MoO^{3-x} film after the Ag$^+$ reducing reaction under the UV-light illumination.

orbit doublets. The two characteristic strong peaks at 230.2 and 232.6 eV can be indexed to Mo^{4+}, and the two weak shoulder peaks at 231.28 and 234.38 eV can be attributed to Mo^{5+}, while the other two weak shoulder peaks at 232.68 and 235.98 eV can be attributed to Mo^{6+}. Furthermore, based on the

integrated area of the specific peak, the percentage of each Mo valence state in the film is calculated. As it indicates that, in the annealed MoO_{3-x} film (Fig. 5c), 23.7% of the Mo ions are at Mo^{6+} state, 48.1% are Mo^{5+} state and 28.2% are Mo^{4+} state. However, in the MoO_{3-x}/Ag NPs film (Fig. 5d), it reveals that 45.5%

Figure 5 The XPS survey spectrum of **a** Annealed MoO_{3-x} film and **b** MoO_{3-x}/Ag NPs film; deconvoluted core level spectra of Mo $3d$ on the **c** surface of annealed MoO_{3-x} film and (d) MoO_{3-x}/Ag NPs film.
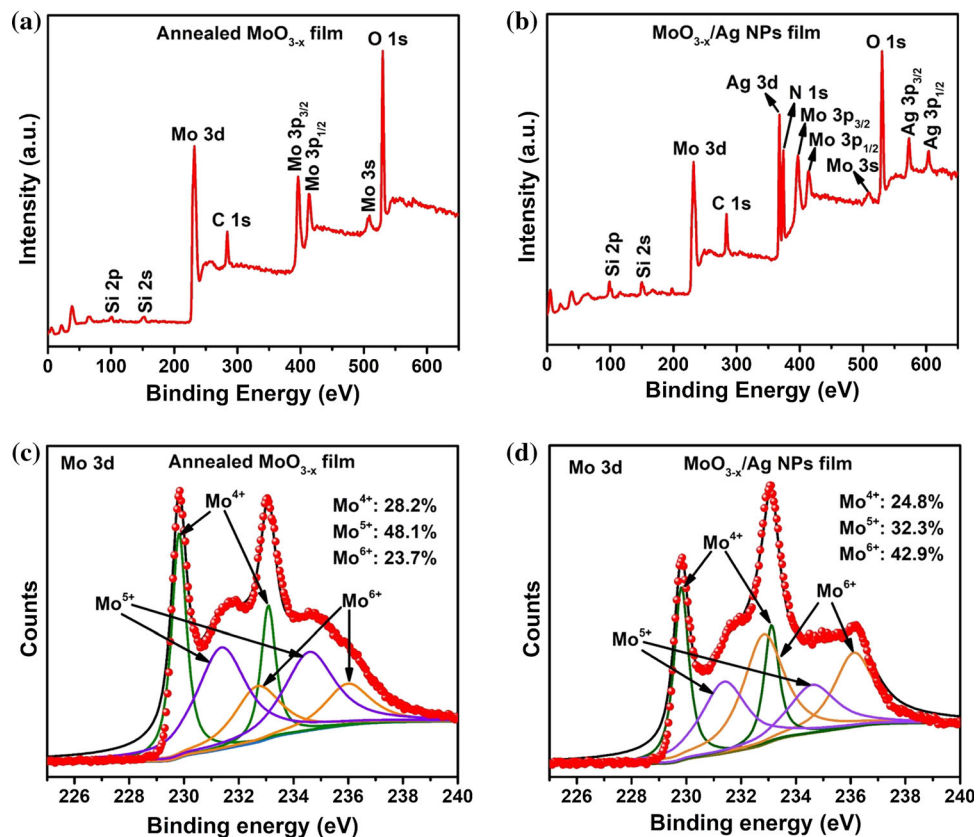

of the Mo ions are at Mo^{6+} state, 29.7% are Mo^{5+} state and 24.8% are Mo^{4+} state. Based on above XPS analysis results, it can be known that part of the low valence state Mo ions in the annealed MoO_{3-x} film are oxidized to high valance states during the UV-light illumination period, which supports the understanding that the low valence state Mo ions in the film act as reducing agents, and consequently facilitate the Ag^+ reducing reaction.

To evaluate the SERS activity of the MoO_{3-x}/Ag NPs film, Rhodamine B (RhB) molecules were used as the Raman reporter. Figure 6a shows the SERS spectra of RhB molecules detected by using MoO_{3-x}/Ag NPs one-layer film synthesized with different $AgNO_3$ solution concentrations. It illustrates that the characteristic peaks of RhB from 600 to 2000 cm^{-1} could be noticeably observed.

Specifically, the Raman peak that locates at 620 cm^{-1} (P1) is attributed to the aromatic banding, while the Raman peak at 1195 cm^{-1} (P2) arises from aromatic $C-H$ banding. In the meanwhile, the Raman peak at 1280 cm^{-1} (P3) arises from C–C bridge bands stretching, and finally the Raman peaks at 1357 (P4) and 1646 cm^{-1} (P5) are ascribed to the

aromatic C–C stretching [57]. Besides, those additional Raman peaks are contributed by the vibrating bonds of the molybdenum oxide, and the peak assignments can be found in Fig. S3, Supplementary Information [45, 54]. Furthermore, from Fig. 6a, it can be observed that 0.18 mg mL^{-1} $AgNO_3$ solution only gives relatively weak Raman signal enhancement when compared to that obtained on the bare MoO_{3-x} film, this observation indicates that the EM supported by the Ag NPs is relatively insignificant as there are inadequate Ag NPs reduced when the $AgNO_3$ solution concentration is low. Subsequently, with the gradual increase in the $AgNO_3$ solution concentration, it shows that the Raman signal intensities remarkably climb up, and ultimately, the maximum Raman signal enhancement is found when the $AgNO_3$ solution concentration reaches 1.8 mg mL^{-1}. This observed significantly Raman signal enhancement is ascribed to the extraordinarily synergetic effect of EM produced by denser Ag NPs and CM.

To further improve the SERS performance of MoO_{3-x}/Ag NPs film, in the subsequent experiment, the MoO_{3-x}/Ag NPs film prepared with
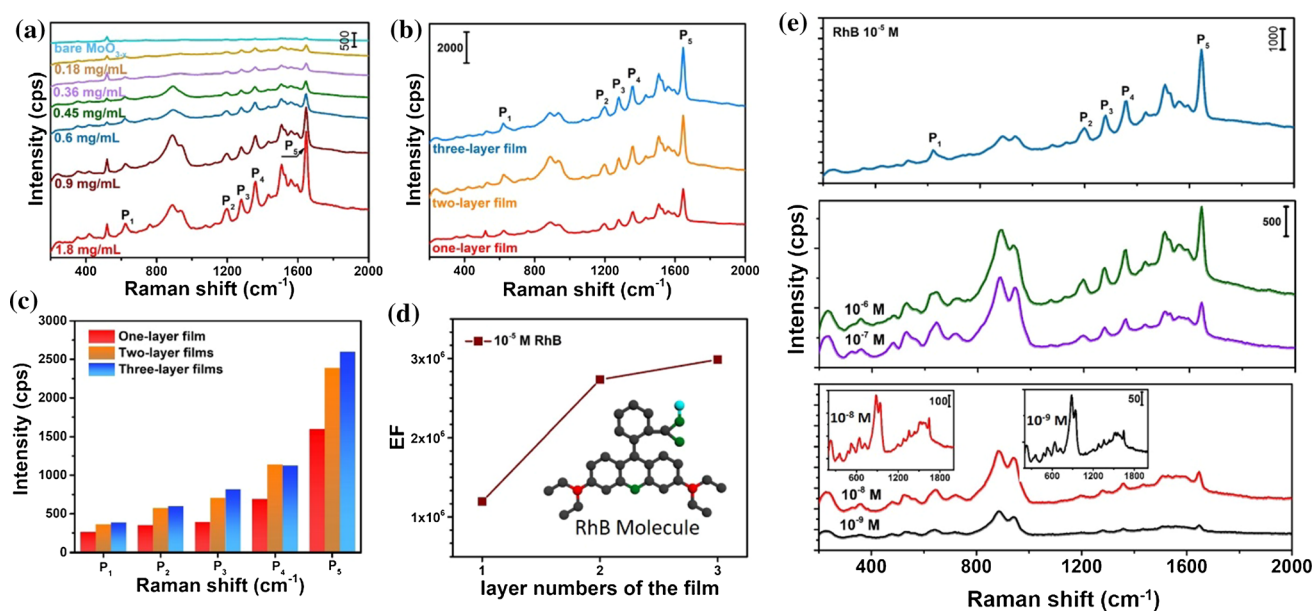
Figure 6 **a** The SERS spectra of the RhB-labelled MoO_{3-x}/Ag NPs synthesized with $AgNO_3$ solutions of 1.8, 0.9, 0.6, 0.45, 0.36 and 0.18 mg mL^{-1}; **b** Raman spectra of RhB molecules (10^{-5} M) collected on MoO_{3-x}/Ag NPs with different layers; **c** The corresponding distributions of Raman spectra with the Raman band at 621, 1193, 1278, 1358 and 1646 cm^{-1}; **d** The evolution of EF as a function of MoO_{3-x}/Ag NPs film layers plotted in logarithmic scale (inset: the structural formula of RhB molecule); **e** Raman spectra collected for MoO_{3-x}/Ag NPs film under five different concentrations, 10^{-5}, 10^{-6}, 10^{-7}, 10^{-8} and 10^{-9} M, suggesting the detection limit was as low as 10^{-9} M (inset: with narrowed y scale for 10^{-8} M and 10^{-9} M).

1.8 mg mL^{-1} $AgNO_3$ solution was chosen as the fundamental unit, and a multi-layer film was constructed by repetitively stacking the unit film on the prior one accordingly to the experimental design (see Fig. 1). The SERS performance of the MoO_{3-x}/Ag NPs multi-layer films was then accessed and the results are shown in Fig. 6b. As it is illustrated that, with different layers of the MoO_{3-x}/Ag NPs films, a multi-stage amplifying of the Raman signal could be observed. More specifically, the intensities of P1, P2, P3, P4 and P5 all are coincidently enhanced. Thereafter, for the purpose of approximating the gain of the MoO_{3-x}/Ag NPs films with different layer numbers, the evolution of each Raman peak intensities (P1, P2, P3, P4 and P5) are extracted when the film layer numbers increase from one to three (Fig. 6c), then the gains of the multi-layer films are calculated. As it can be seen that, for the MoO_{3-x}/Ag two-layer NPs films, the peak heights of P1, P2, P3, P4 and P5 are about 1.37, 1.63, 1.80, 1.65 and 1.50 times higher when they compare to those observed on the MoO_{3-x}/Ag NPs one-layer film, while with the further increase in the layer number to three, the peak heights at P1, P2, P3, P4 and P5 are about 1.47, 1.70, 2.07, 1.63 and 1.64 times higher than those observed

on the MoO_{3-x}/Ag NPs one-layer film. At this moment, it could be found that the multi-stage amplifying is weakened when the layer numbers increase from two to three. In consideration of the Raman enhancement mechanism, a solid understanding is ascribed to the boosted surface electromagnetic field induced by the stacked Ag NPs, however, when the layer numbers of the films increase, the distance between those lower layer Ag NPs and the analytes is also enlarged, and as a short-range enhancement effect, the EM contributed by these lower layer Ag NPs is severely weakened. In addition, this amplifying capability is also limited by the maximum laser penetration depth. When the film layers increase, those Ag NPs deeply buried in the oxides can't receive the incident light, and consequently there is no electromagnetic field contributions from these Ag NPs, thus even more Ag NPs are involved in the stacked structure when the layer numbers increase, the Raman signal intensities won't proportionally enhanced.

In the next discussion, the EFs of the above three different layer-number films are calculated. During the calculation, the integrated peak intensity at 1646 cm^{-1} was used to determine the EFs (details in

the Supplementary Information). As shown in Fig. 6d, it can be found that the respective EFs are 1.195×10^6, 2.733×10^6 and 2.985×10^6 for three structures with different layers, which are comparable to those EFs obtained on metal oxide-noble-metal nanoparticles composites (Table 1). Additionally, the detection limit of the MoO_{3-x}/Re Ag NPs films was also evaluated. To achieve this, the Raman spectra of different RhB concentrations were measured by averaging fifteen measurement points. Figure 6e shows the Raman spectra of different RhB concentrations, decreasing from 10^{-5}, 10^{-6}, 10^{-7}, 10^{-8} to 10^{-9} M. Clearly, it could be found that Raman signal of RhB at 10^{-9} M on the three-layer MoO_{3-x}/Re Ag NPs films are still observable (inset in Fig. 6e), which gives the approximated lower detection limit of this three-layer film to be 10^{-9} M. At this stage, it is worth noting that only such a low detection limit enables the high sensitivity detection of extremely low trace analytes.

Furthermore, as it is known to all that the uniformity of the Raman signal intensities from the SERS-active substrate is an important aspect in the quantitative detection. Therefore, in the subsequent experiment, the Raman signal intensity mappings were measured on all three films with different layer numbers. Typically, a randomly selected 100×100 μm^2 square was used to perform the mapping measurement, and totally 2500 measurement points were recorded for each film by using the 10^{-5} M RhB as reporter. Figure 7 shows the mapping data of the Raman peak intensities at 1646 cm^{-1}. It can be observed in Fig. 7a that the average mapping intensity obtained from MoO_{3-x}/Re Ag NPs one-

layer film is 1119.6 cps. Meanwhile, for the films with MoO_{3-x}/Re Ag NPs two- and three-layer film, the respective average Raman mapping signal intensities are 2008.8 and 2196.8 cps. Moreover, the relative standard derivations (RSD) for the three films were also calculated. As shown in Fig. 7, they are 26.73%, 13.4% and 7.54% for one-layer, two-layer and three-layer film, respectively. Based on the above results, it is found that all three prepared structures show attractive Raman signal intensity enhancements, and more interestingly, it can be observed that the RSD is also significantly improved with the increase in the film layer numbers, which could be ascribed to the improved average Ag coverage when more layers are built.

In the end, to understand the layer-dependent SERS performance of the MoO_{3-x}/Ag NPs films, FDTD simulation was performed to investigate the surface electromagnetic field profile around the Ag NPs. By carefully analyzing the SEM images (Fig. S2, and Fig. S4, Supplementary Information), it can be found that the Ag NPs show hydrangea-like shapes with notable walls on the surface. And in consideration of reaching a compromise between the actual morphologies of the Ag NPs and the efficiency of the calculation, the Ag NPs were imitated by a 270-nm radius of Ag sphere decorated with 130-nm height and 15-nm thickness of surficial walls in the calculation (Fig. S5, Supplement Information). Moreover, the lateral distance between the Ag NPs on the same layer was set to 120 nm, whereas the vertical distance of the two Ag NPs on the nearby layer was set to 110 nm. The simulation results are shown in Fig. 8. Obviously, it could be observed on the one-layer film

Table 1 Summary of the SERS performance of metal oxide and metal oxide-noble metal nanoparticle composites [29, 36–38, 45, 47, 48, 58]

Substrate	Raman reporter and excited wavelength	EF and LOD	References
$W_{18}O_{49}$ film	Rhodamine 6G; 532 nm	3.4×10^5; 10^{-7} M	[29]
MoO_2 film	Rhodamine 6G; 532 nm	3.75×10^6; 10^{-7} M	[36]
Cu_2O nanospheres	4-Mercaptobenzoic Acid; 488 nm	5.36×10^5; NA	[37]
Ar^+ ion irradiated TiO_2 film	Rhodamine 6G; 532 nm	4.5×10^5; 10^{-8} M	[38]
MoO_x-AuNSs hybrid	IR-780 iodide; 785 nm	1.7×10^5; NA	[45]
Ag-TiO_2 nanorods	Rhodamine 6G; 514 nm	10^5; NA	[47]
Au-TiO_2 nanocomposites	4-Mercaptobenzoic Acid; 633 nm	0.7×10^4; 10^{-8} M	[48]
Au-Coated ZnO Nanorods	Methylene Blue; 632.8 nm	3.4×10^5; 10^{-12} M	[58]
MoO_{3-x}/Ag NPs three-layer film	Rhodamine B; 532 nm	2.985×10^6; 10^{-9} M	This work
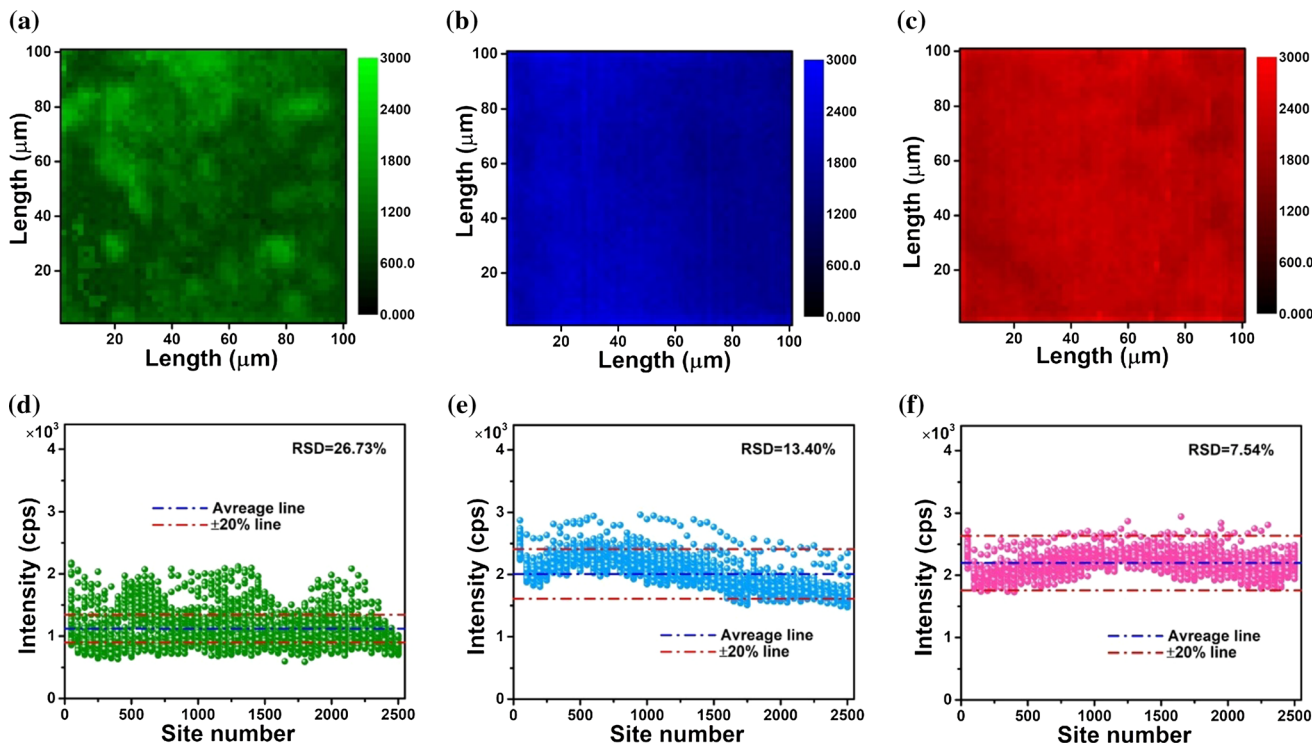
Figure 7 Raman mapping intensity at 1646 cm^{-1} obtained on a 100 × 100 μm^2 square with 10^{-5} M RhB as the reporter **a** one-layer, **b** two-layer and **c** three-layer film; **d** the RSD of the Raman mapping intensities for the three different films.

One-layer film   Two-layer film   Three-layer film
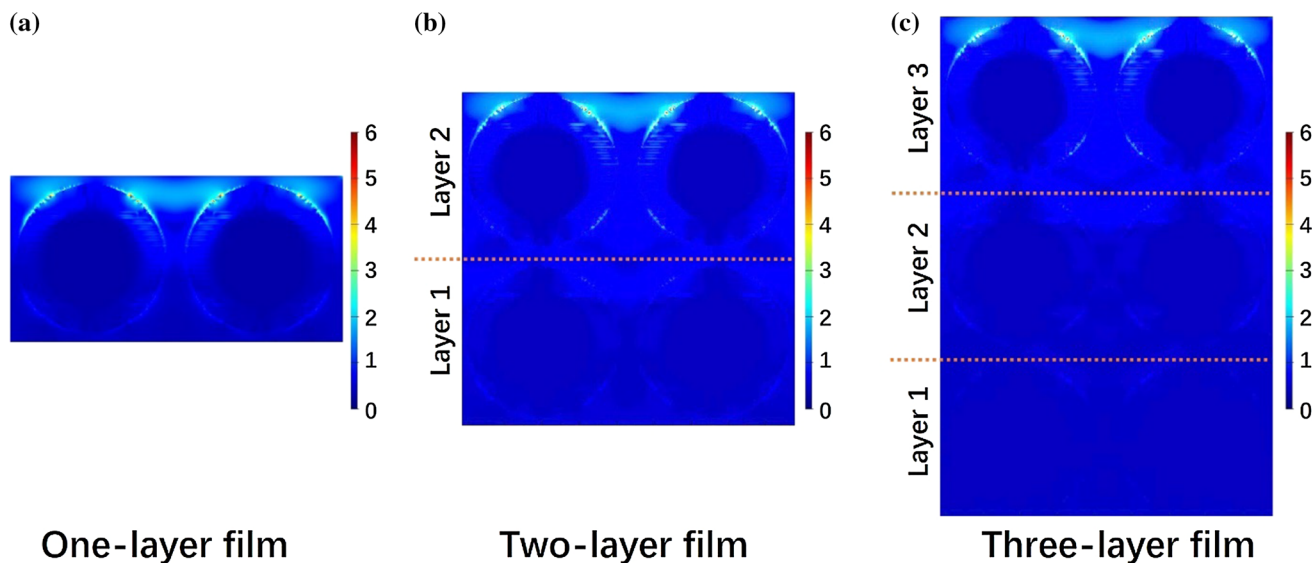
Figure 8 The E-field intensity profile on the Ag NPs when the incident laser wavelength is 532 nm. **a** one-layer; **b** two-layer and **c** three-layer film.

that strong surface electromagnetic fields are generated on the walls of the Ag NPs due the excitation of the localized surface plasmon resonance by the incident light, and in the meanwhile, very weak "hots pots" are also observed within the gap of the closely

arrayed Ag NPs. In the meanwhile, for the two-layer film, similar surface electromagnetic field profile and "hot spots" also can be found on the top layer of Ag NPs. In addition, on the lower surface of the top Ag NPs (Layer 2) and the upper surface of the bottom Ag

NPs (Layer 1), extra strong surface electromagnetic field is excited due to the interaction between the light and Ag NPs. Lastly, for the three-layer film, same as one-layer and two-layer film, surface electromagnetic field profile and "hot spots" are observed on the top layer of Ag NPs, and moreover, additional strong surface electromagnetic field is also excited on the lower surface of the top Ag NPs (Layer 3) and the upper surface of the middle Ag NPs (Layer 2). However, due to the limitation of the light penetration depth, only very weak surface electromagnetic field is observed within gap between the middle layer (Layer 2) and the bottom layer (Layer 1), which complies with the experimental evidence that very weak Raman amplifying is observed when the film reaches three layers.

Conclusion

To summarize, it is demonstrated an easy-fabricating SERS substrate based on the MoO_{3-x}/Ag NPs film. Experimental investigations evidence that the prepared MoO_{3-x}/Ag NPs film show superior SERS performance supported by the joint enhancement mechanism of EM and CM. Moreover, by constructing multi-layer films, from one to three layers, it demonstrates a multi-stage amplifying strategy. More specifically, for MoO_{3-x}/Ag NPs three-layer film, it gives about 2.07 times gain of the Raman intensity (1280 cm^{-1}) compared to that of MoO_{3-x}/Ag NPs one-layer film. Finally, it is also demonstrated that the MoO_{3-x}/Ag NPs films show relatively good uniformity of the SERS signal in a large area, which is verified by the mapping measurement. Overall, this work presents a high EFs and uniform SERS sensor with the MoO_{3-x}/Ag NPs multi-layer films, and it is expected that this sensor can be potentially used in future for ultra-low trace molecular analysis applications.

Acknowledgement

Authors contribution

All authors contributed equally. And all authors have given approval to the final version of the manuscript.

Compliance with ethical standards

Conflict of interest The authors declare that they have no conflict of interest.

Electronic supplementary material: The online version of this article (https://doi.org/10.1007/s10853-020-04669-5) contains supplementary material, which is available to authorized users.

References

[1] Ding S-Y, Yi J, Li J-F, Ren B, Wu D-Y, Panneerselvam R, Tian Z-Q (2016) Nanostructure-based plasmon-enhanced raman spectroscopy for surface analysis of materials. Nat Rev Mate 1:16021-1–16021-16

[2] Laing S, Jamieson LE, Faulds K, Graham D (2017) Surface-enhanced Raman spectroscopy for in-vivo biosensing. Nat. Rev. Chem. 1:0060-1–0060-19

[3] Li J-F, Zhang Y-J, Ding S-Y, Panneerselvam R, Tian Z-Q (2017) Core-shell nanoparticle-enhanced Raman spectroscopy. Chem Rev 117:5002–5069

[4] Reguera J, Langer J, Jiménez de Aberasturi D, Liz-Marzán LM (2017) Anisotropic metal nanoparticles for surface enhanced Raman scattering. Chem Soc Rev 46:3866–3885

[5] Niu W, Chua YAA, Zhang W, Huang H, Lu X (2015) Highly symmetric gold nanostars: crystallographic control and surface-enhanced Raman scattering property. J Am Chem Soc 137:10460–10463

[6] Liu K, Bai Y, Zhang L et al (2016) Porous Au–Ag nanospheres with high-density and highly accessible hotspots for SERS analysis. Nano Lett 16:3675–3681

[7] Ye S, Benz F, Wheeler MC et al (2016) One-step fabrication of hollow-channel gold nanoflowers with excellent catalytic performance and large single-particle SERS activity. Nanoscale 8:14932–14942

[8] Zhu C, Meng G, Zheng P et al (2016) A hierarchically ordered array of silver-nanorod bundles for surface-enhanced

Raman scattering detection of phenolic pollutants. Adv Mater 28:4871–4876

[9] Tian Y, Liu H, Chen Y et al (2019) Seedless one-spot synthesis of 3D and 2D Ag Nanoflowers for multiple phase SERS-based molecule detection. Sens Actuators B: Chem 301:127142(1–13)

[10] Ashley MJ, Bourgeois MR, Murthy RR et al (2018) Shape and size control of substrate-grown gold nanoparticles for surface-enhanced Raman spectroscopy detection of chemical analytes. J Phys Chem C 122:2307–2314

[11] He S, Kyaw YME, Tan EKM et al (2018) Quantitative and label-free detection of protein kinase a activity based on surface-enhanced Raman spectroscopy with gold nanostars. Anal Chem 90:6071–6080

[12] Xu J, Wu D, Li Y, Xu J, Gao Z, Song Y-Y (2018) Plasmon-triggered hot-spot excitation on SERS substrates for bacterial inactivation and in situ monitoring. ACS Appl Mater Interfaces 10:25219–25227

[13] Zhu C, Du D, Eychmüller A, Lin Y (2015) Engineering ordered and nonordered porous noble metal nanostructures: synthesis, assembly, and their applications in electrochemistry. Chem Rev 115:8896–8943

[14] Lv W, Gu C, Zeng S, Han J, Jiang T, Zhou J (2018) One-pot synthesis of multi-branch gold nanoparticles and investigation of their SERS performance. Biosensors 8:113(1–10)

[15] Ma W, Fu P, Sun M, Xu L, Kuang H, Xu C (2017) Dual quantification of MicroRNAs and telomerase in living cells. J Am Chem Soc 139:11752–11759

[16] Zhang J, Li X, Sun X, Li Y (2005) Surface enhanced Raman scattering effects of silver colloids with different shapes. J. Phys. Chem. B 109:12544–12548

[17] Jiang T, Chen G, Tian X, Tang S, Zhou J, Feng Y, Chen H (2018) Construction of long narrow gaps in Ag nanoplates. J Am Chem Soc 140:15560–15563

[18] Li H, Yang Q, Hou J, Li Y, Li M, Song Y (2018) Bioinspired micropatterned superhydrophilic Au-areoles for surface-enhanced Raman scattering (SERS) trace detection. Adv Funct Mater 28:1800448(1–7)

[19] Liu Z (2017) One-step fabrication of crystalline metal nanostructures by direct nanoimprinting below melting temperatures. Nat Commun 8:14910(1–7)

[20] Yin G, Bai S, Tu X et al (2019) Highly sensitive and stable SERS substrate fabricated by Co-sputtering and atomic layer deposition. Nanoscale Res Lett 14:168

[21] Zhou S, Zhao M, Yang T-H, Xia Y (2019) Decahedral nanocrystals of noble metals: synthesis, characterization, and applications. Mater Today 22:108–131

[22] Sun L, Yu Z, Lin M (2019) Synthesis of polyhedral gold nanostars as surface-enhanced raman spectroscopy substrates

for measurement of thiram in peach juice. Analyst 144:4820–4825

[23] Cao Y-Q, Qin K, Zhu L, Qian X, Zhang X-J, Wu D, Li A-D (2017) Atomic-layer-deposition assisted formation of wafer-scale double-layer metal nanoparticles with tunable nanogap for surface-enhanced Raman scattering. Sci. Rep 7:5161(7–8)

[24] Matricardi C, Hanske C, Garcia-Pomar JL, Langer J, Mihi A, Liz-Marzán LM (2018) Gold nanoparticle plasmonic superlattices as surface-enhanced Raman spectroscopy substrates. ACS Nano 12:8531–8539

[25] Zhou S, Li J, Gilroy KD et al (2016) Facile synthesis of silver nanocubes with sharp corners and edges in an aqueous solution. ACS Nano 10:9861–9870

[26] Lin D, Wu Z, Li S et al (2017) Large-area au-nanoparticle-functionalized Si nanorod arrays for spatially uniform surface-enhanced Raman spectroscopy. ACS Nano 11:1478–1487

[27] Chen H-C, Hsu T-C, Liu Y-C, Yang K-H (2014) Surfactant-assisted preparation of surface-enhanced Raman scattering-active substrates. RSC Adv. 4:10553–10559

[28] Wall MA, Harmsen S, Pal S et al (2017) Surfactant-free shape control of gold nanoparticles enabled by unified theoretical framework of nanocrystal synthesis. Adv Mater 29:1605622(1–8)

[29] Cong S, Yuan Y, Chen Z et al (2017) Noble metal-comparable SERS enhancement from semiconducting metal oxides by making oxygen vacancies. Nat Commun 6:7800(1–7)

[30] Zheng Z, Cong S, Gong W et al (2017) Semiconductor SERS enhancement enabled by oxygen incorporation. Nat Comm 8:1993(1–10)

[31] Zhou C, Sun L, Zhang F et al (2019) Electrical tuning of the SERS enhancement by precise defect density control. ACS Appl Mater Interfaces 11:34091–34099

[32] Wu H, Wang H, Li G (2017) Metal oxide semiconductor SERS-active substrates by defect engineering. Analyst 142:326–335

[33] Johansson MB, Mattsson A, Lindquist S-E, Niklasson GA, Österlund L (2017) The importance of oxygen vacancies in nanocrystalline WO_{3-x} thin films prepared by DC magnetron sputtering for achieving high photoelectrochemical efficiency. J Phys Chem C 121:7412–7420

[34] Sun L, Hu H, Zhan D et al (2014) Plasma modified MoS_2 nanoflakes for surface enhanced Raman scattering. Small 10:1090–1095

[35] Lu Z, Si H, Li Z et al (2018) Sensitive, reproducible, and stable 3D plasmonic hybrids with bilayer WS_2 as nanospacer for SERS analysis. Opt Express 26:21626(1–6)

[36] Zhang Q, Li X, Ma Q et al (2017) A metallic molybdenum dioxide with high stability for surface enhanced Raman spectroscopy. Nat Commun 8:14093

[37] Jiang L, You T, Yin P, Shang Y, Zhang D, Guo L, Yang S (2013) Surface-enhanced Raman scattering spectra of adsorbates on Cu_2O Nanospheres: charge-transfer and electromagnetic enhancement. Nanoscale 5:2784–2789

[38] Zheng X, Ren F, Zhang S et al (2017) A general method for large-scale fabrication of semiconducting oxides with high SERS sensitivity. ACS Appl Mater Interfaces 9:14534–14544

[39] Prabhu BR, Bramhaiah K, Singh KK, John NS (2019) Single sea Urchin–MoO_3 nanostructure for surface enhanced Raman spectroscopy of dyes. Nanosc Adv 1:2426–2434

[40] Zhan Y, Liu Y, Zu H et al (2018) Phase-controlled synthesis of molybdenum oxide nanoparticles for surface enhanced Raman scattering and photothermal therapy. Nanoscale 10:5997–6004

[41] Song G, Shen J, Jiang F et al (2014) Hydrophilic molybdenum oxide nanomaterials with controlled morphology and strong plasmonic absorption for photothermal ablation of cancer cells. ACS Appl Mater Interfaces 6:3915–3922

[42] Li R, An H, Huang W, He Y (2018) Molybdenum oxide nanosheets meet ascorbic acid: tunable surface plasmon resonance and visual colorimetric detection at room temperature. Sens Actuators B: Chem 259:59–63

[43] Wang J, Yang Y, Li H et al (2019) Stable and tunable plasmon resonance of molybdenum oxide nanosheets from the ultraviolet to the near-infrared region for ultrasensitive surface-enhanced Raman analysis. Chem Sci 10:6330–6335

[44] Zhang BY, Zavabeti A, Chrimes AF et al (2018) Degenerately hydrogen doped molybdenum oxide nanodisks for ultrasensitive plasmonic biosensing. Adv Funct Mater 28:1706006

[45] Guo Y, Zhuang Z, Liu Z et al (2019) Facile hot spots assembly on molybdenum oxide nanosheets via in situ decoration with gold nanoparticles. Appl Surf Sci 480:1162–1170

[46] Liang X, Zhang X-J, You T-T, Wang G-S, Yin P-G, Guo L (2016) Controlled assembly of one-dimensional MoO_3@Au hybrid nanostructures as SERS substrates for sensitive melamine detection. CrystEngComm 18:7805–7813

[47] Kumar S, Lodhi DK, Singh JP (2016) Highly sensitive multifunctional recyclable Ag–TiO_2 nanorod SERS substrates for photocatalytic degradation and detection of dye molecules. RSC Adv 6:45120–45126

[48] Jiang X, Sun X, Yin D et al (2017) Recyclable Au–TiO_2 nanocomposite SERS-active substrates contributed by synergistic charge-transfer effect. Phys Chem Chem Phys 19:11212–11219

[49] Huang J, Ma D, Chen F, Chen D, Bai M, Xu K, Zhao Y (2017) Green in situ synthesis of clean 3D chestnutlike Ag/WO_{3-x} nanostructures for highly efficient, recyclable and sensitive SERS sensing. ACS Appl Mater Interfaces 9:7436–7446

[50] Zhou YF, Bi K, Wan L et al (2015) Enhanced adsorption and photocatalysis properties of molybdenum oxide ultrathin nanobelts. Mate. Lett. 154:132–135

[51] Su L, Xiong Y, Chen Z, Duan Z, Luo Y, Zhu D, Ma X (2019) MoO_3 nanosheet-assisted photochemical reduction synthesis of Au nanoparticles for surface-enhanced Raman scattering substrates. Sens Actuators B: Chem 279:320–326

[52] Yuksel R, Coskun S, Unalan HE (2016) Coaxial silver nanowire network core molybdenum oxide shell supercapacitor electrodes. Electrochim Acta 193:39–44

[53] Huang Q, Hu S, Zhuang J, Wang X (2012) MoO_{3-x}-based hybrids with tunable localized surface plasmon resonances: chemical oxidation driving transformation from ultrathin nanosheets to nanotubes. Chem Eur J 18:15283–15287

[54] Fodjo EK, Li D-W, Marius NP, Albert T, Long Y-T (2013) Low temperature synthesis and SERS application of silver molybdenum oxides. J Mater Chem A 1:2558–2566

[55] Kleinman SL, Frontiera RR, Henry A-I, Dieringer JA, Van Duyne RP (2013) Creating, characterizing, and controlling chemistry with SERS hot spots. Phys Chem Chem Phys 15:21–36

[56] Cheng H, Kamegawa T, Mori K, Yamashita H (2014) Surfactant-free nonaqueous synthesis of plasmonic molybdenum oxide nanosheets with enhanced catalytic activity for hydrogen generation from ammonia borane under visible light, Angew. Chem Int Ed 53:2910–2914

[57] Lin S, Hasi W-L-J, Lin X et al (2015) Rapid and sensitive SERS method for determination of rhodamine B in chili powder with paper-based substrates. Anal Methods 7:5289–5294

[58] Sinha G, Depero LE, Alessandri I (2011) Recyclable SERS substrates based on Au-Coated ZnO nanorods. ACS Appl Mater Interfaces 3:2557–2563